THE JOURNAL OF PHYSICAL CHEMISTRY C
Article
Cite This: *J. Phys. Chem. C* 2019, 123, 8908−8922
pubs.acs.org/JPCC

Spatially Resolved Product Speciation during Struvite Synthesis from Magnesite ($MgCO_3$) Particles in Ammonium (NH_4^+) and Phosphate (PO_4^{3-}) Aqueous Solutions

Baoying Lu,[†,‡] Daniyal Kiani,[†] William Taifan,[†] Dovydas Barauskas,[†] Kenneth Honer,[†] Lihua Zhang,[§] and Jonas Baltrusaitis*[,†]

[†]Department of Chemical and Biomolecular Engineering, Lehigh University, B336 Iacocca Hall, 111 Research Drive, Bethlehem, Pennsylvania 18015, United States

[‡]Medical College, Guangxi University of Science and Technology, 1301 Medical Building, 257 Liushi Street, Liuzhou, Guangxi 545000, China

[§]Center for Functional Nanomaterials, Brookhaven National Laboratory, Upton, New York 11973, United States

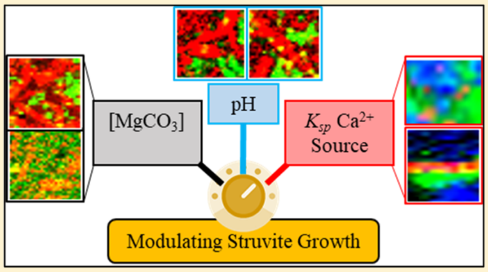

ABSTRACT: While population growth necessitates a significant increase in crop production, stringent environmental regulations require that it be done using sustainable nutrient sources. Nutrients in the form of NH_4^+ and PO_4^{3-} are recovered from wastewater streams via precipitation, using water-soluble magnesium ions to form sustainable, slow-release fertilizer, struvite ($MgNH_4PO_4{\cdot}6H_2O$). However, the magnesium needed is mainly incorporated in the crystal lattices of very low-solubility minerals. This work utilizes a combination of powder X-ray diffraction (pXRD) and ex situ Raman and energy-dispersive X-ray spectroscopies combined with ion chromatography to characterize transformation products of low-solubility $MgCO_3$ particles in NH_4^+- and PO_4^{3-}- containing aqueous solutions with and without Ca^{2+} ions present. Although pXRD showed struvite as the predominant solid product for the molar ratio $[Mg^{2+}/NH_4^+/PO_4^{3-}]$ of [0.2:1:1] and higher, ex situ Raman spectra evidenced formation of a dypingite-like phase along with struvite. Single-crystal Raman spectroscopy in combination with scanning transmission electron microscopy/energy-dispersive X-ray spectroscopy showed Ca^{2+} incorporation into the structure of struvite crystals as submicron crystallites at the Ca^{2+}/Mg^{2+} ratio of 0.2, from both $CaCO_3$ and $CaCl_2$ and at the Ca^{2+}/Mg^{2+} ratio of 1, in the case of $CaCO_3$. Moreover, distinct solid product speciation was observed when Ca^{2+} was present in aqueous solutions when using $CaCl_2$; for example, hydroxyapatite was observed for $Ca^{2+}/Mg^{2+} = 1$ when $CaCl_2$ was used. The results reported here unravel the effect of the physicochemical solution parameters, such as concentration of $MgCO_3$, pH, Ca^{2+} concentration, and solubility of Ca-containing precursors, on the formation of struvite crystals. This shows that recovery of nutrients containing N and P from wastewater streams is possible in the form of a slow-release fertilizer (struvite) using low-solubility, abundant magnesium-containing minerals.

■ INTRODUCTION

The importance of sustainable, slow-release fertilizers is highlighted by the fact that increasing crop and livestock production has resulted in a major influx of nitrogen (N) and phosphorus (P) into the environment because of increased synthetic fertilizer use.[1] N fertilizers have a large environmental footprint, as they are produced via NH_3 synthesis, which consumes about 1−2% of the total global energy and 3−5% of total natural gas.[2,3] Such N fertilizers are highly water soluble and lead to release of large amounts of soluble forms of N to the soil upon application. The surplus N is lost to the environment in the form of greenhouse gas emissions, such as ammonia (NH_3), nitrous oxide (N_2O), nitric oxide (NO),[4,5] or aqueous NH_4^+ and NO_3^- ions, whereas surplus P, being much less soluble, enters the watershed causing hazardous eutrophication or accumulates in soil.[6−9] Additionally, large amounts of wastewater enters watershed in the form of sewage effluents and agricultural runoff. Such wastewater is rich in NH_4^+ and PO_4^{3-}, which then encounter natural mineral surfaces containing magnesium (Mg) and calcium (Ca) and can potentially react to form solid products.

To produce sustainable, slow-release fertilizers for the ever-increasing demand, reactions of natural minerals, such as the magnesium-containing magnesite, ($MgCO_3$), with ammonium and phosphate (NH_4^+ and PO_4^{3-}) ions present in water streams to synthesize struvite ($MgNH_4PO_4{\cdot}6H_2O$) are of major importance. In particular, struvite crystallizes if pH of the solution is 8.0−9.0.[10,11] Struvite crystal growth using water-soluble magnesium salts depends on many conditions, including pH,[12] solution saturation with NH_4^+ and PO_4^{3-},[13] and presence of other cations, such as Ca^{2+}.[14] However, magnesium, although a common constituent of many complex

Received: December 20, 2018
Revised: March 21, 2019
Published: March 21, 2019

ACS Publications

DOI: 10.1021/acs.jpcc.8b12252
J. Phys. Chem. C 2019, 123, 8908−8922

minerals comprising 2% of the Earth's crust, is mostly incorporated in the crystal lattice of low-solubility minerals that typically undergo slow surface reaction/hydration.[15] Interactions of these sparingly soluble magnesium oxides or carbonates with aqueous NH_4^+ and PO_4^{3-} ions proceed via a surface reaction limited mechanism.[16] There is a limited number of experimental studies that spectroscopically measured the surface reactivity of such sparingly soluble Mg-containing mineral surfaces toward NH_3, NH_4^+,[17,18] and PO_4^{3-}[19−22] and studied the resulting solid product speciation. Sparingly soluble MgO has been studied for solution phase synthesis in various literature reports and has shown to be very reactive toward various anions in high relative humidity conditions. The reactivity of the MgO crystalline surface was explained by the presence of ∼2 monolayers of adsorbed H_2O,[23,24] as inferred from transmission Fourier-transform infrared spectroscopy measurements. The ideal MgO(100) surface is by far energetically predominant and only partially dissociates H_2O[25] but the extended defects, such as mono- and diatomic steps, will readily chemisorb H_2O, yielding a series of one, two-, or four-fold coordinate hydroxyl groups.[26] Although the strength of water adsorption is primarily driven by the coordination number of the surface acid−base pairs, the surface hydroxyl groups resulting from water dissociation are also considerably stabilized by the electrostatic interaction with coadsorbed protons.[27] At low coverage, such an interaction, considerably stronger than hydrogen bonding, hinders any proton diffusion away from its neighboring hydroxyl groups. The diverse chemical environment produced as a result of these hydroxyl (OH^-) groups alters MgO surface reactivity.[28] Surface sites exhibiting varying degrees of basicity are formed, with water O−H bond breakage occurring only at strongly basic edge sites[29] and nondissociative H_2O adsorption taking place on medium-strength basic terrace sites.[30] Moreover, it is known that hydroxyl groups will dominate the MgO and $MgCO_3$ surfaces in aqueous solutions and act as hosts for the struvite precursor ions, such as NH_4^+ and PO_4^{3-}.[31,32] At pH 9 under room temperature, equal amounts of NH_3 and NH_4^+ are present in an aqueous environment.[33] Moreover, under such conditions, NH_3/NH_4^+ will be weakly adsorbed on hydrated MgO or $MgCO_3$ by hydrogen-bonding of the nitrogen atom to hydroxyl groups exposed on the surface.[18,34]

On the other hand, strong PO_4^{3-} adsorption in the infrared spectrum was observed on MgO from aqueous solutions with a spectral peak at 1060 cm^{-1} assigned to PO_4^{3-} stretch,[22] likely via surface inner-sphere complexation, surface electrostatic attraction, and precipitation mechanisms.[21] Magnesite ($MgCO_3$) fundamental interactions with NH_4^+ and PO_4^{3-} ions are much less studied and understood compared to MgO. Recent work by Kirinovic et al.[35] utilized ex situ Raman spectroscopy of the solid phase struvite formed using $MgCO_3$ particles and observed precursor concentration dependence of struvite formation kinetics. The combination of powder X-ray diffraction (pXRD) and Raman and SEM data suggested that at low NH_4^+ and PO_4^{3-} concentrations, a reactive intermediate—an amorphous hydroxylated material resembling $Mg(OH)_2$—formed in addition to struvite crystals. Recently, a report containing spatially resolved ex situ Raman and pXRD data and using a MgO precursor showed formation of several solid products including crystalline struvite ($MgNH_4PO_4{\cdot}6H_2O$) and magnesium phosphate ($Mg_3PO_4{\cdot}22H_2O$) and a new amorphous intermediate species present.[16] More importantly, the Raman spectrum of the intermediate compound in this study was assigned to dypingite—$Mg_5(CO_3)_4(OH)_2{\cdot}5H_2O$. This suggested that a parallel hydration reaction of MgO took place and implied that various carbonates of magnesium can potentially react faster with aqueous NH_4^+ and PO_4^{3-} ions than MgO itself.

Although vibrational spectroscopy can provide an in-depth characterization of the material surface and its corresponding binding information, reactive pathways of the NH_4^+ and PO_4^{3-} on magnesium mineral surfaces have yet to be fully elucidated. In the present study, we report insights into the interaction of $MgCO_3$ particles with aqueous NH_4^+ and PO_4^{3-} (fixed 1:1 molar ratio). Ion Chromatography (IC) was utilized to evaluate temporal concentration of the residual ions in solution. Ex situ Raman spectroscopy was used to spatially resolve the solid products, whereas pXRD was employed to evaluate the crystallinity of the solid phase. Finally, Raman/pXRD/energy dispersive X-ray spectroscopy (EDXS) in conjunction with scanning transmission electron microscopy (STEM) studies were performed to examine how calcium ions from either soluble $CaCl_2$ or very low-solubility $CaCO_3$ alter reactive intermediates and affect the resulting solid product speciation.

EXPERIMENTAL METHODS

Ion Chromatography. The Metrohm Eco 925 IC system (Herisau, Switzerland) was used in all experiments. The separation columns used were Metrosep A supp 4/5 guard column (5 × 4 mm) and Metrosep A supp 5 (4 × 150 mm) for anion analysis and Metrosep C 4 guard column (5 × 4 mm) and Metrosep C 4 (4 × 150 mm) for cation analysis. The sample-loop volume was 10 μL in the cation system and 20 μL in the anion system, and the eluted species were measured using a conductivity detector. HNO_3 (1.75 nM) and dipicolinic acid (DPA, 0.7 mM) was used as eluent for Metrosep C 4, whereas 3.2 mM Na_2CO_3 and 1.0 mM $NaHCO_3$ were used for Metrosep A supp 5. All samples were measured at room temperature. Error bars are provided for triplicate in selected experiments. The system was computer controlled through MagIC Net 3.2 software.

Powder X-ray Diffraction. Crystalline nature of all reactants and products was confirmed using pXRD (Empyrean, PANalytical B.V.). The applied current was 40 mA, and the applied voltage was 45 kV. The X-ray mirror that was used was a graded, flat Bragg−Brentano HD mirror, and the step size that was used for the measurements was 0.0131°.

Scanning Transmission Electron Microscopy. The morphology of the catalyst particles was investigated using a dedicated Scanning Transmission Electron Microscope (Hitachi 2700C) operating at 200 kV. The EDXS signals were collected using a Bruker SDD EDX detector with a 30 mm^2 collection window.

Raman Spectroscopy. Ex situ Raman spectra and spectral maps were acquired using WITec alpha300R confocal Raman microscope using 532 nm laser and a ×100 objective. Laser intensity at the sample was ∼54 mW. Spectral maps were typically acquired using 2 s exposure time per single scan point. Two types of Raman spectral maps were obtained. In particular, for $MgCO_3/NH_4H_2PO_4$ experiments, 2-D spectra maps were acquired in the $x-y$ plane, for example, perpendicular to the laser beam. To elucidate homogeneity of a single crystal formed using $MgCO_3/NH_4H_2PO_4$ in the presence of Ca^{2+} ions from $CaCO_3$, 2-D spectral maps were

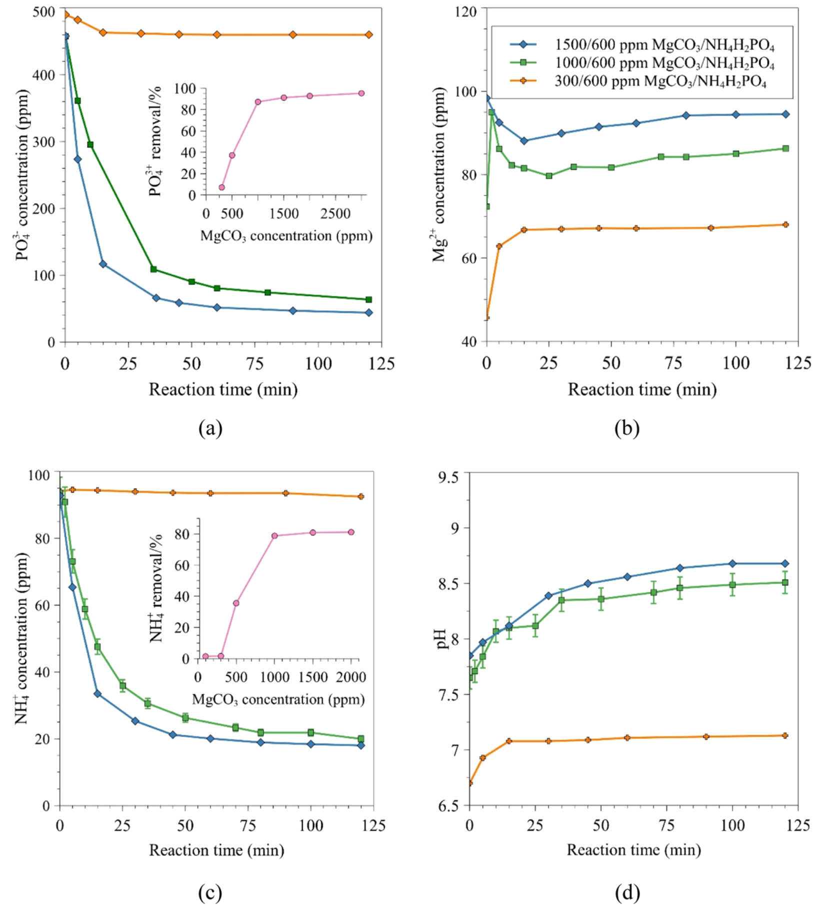

Figure 1. Measured temporal profiles of (a) PO$_4^{3-}$, (b) Mg^{2+}, and (c) NH$_4^+$. Removal of PO$_4^{3-}$ and NH$_4^+$ as a function of MgCO$_3$ concentration (100, 300, 500, 1000, 1500, and 2000 ppm MgCO$_3$) after 120 min of reaction are shown in insets of (a,c), respectively. (d) pH change as a function of reaction time, after addition of 300, 1000, and 1500 ppm MgCO$_3$ with 600 NH$_4$H$_2$PO$_4$. pH before any MgCO$_3$ was added was 5.4.

acquired in the *x*−*z* plane, for example, parallel to the direction of the beam.

The true component analysis (TCA) was used to create spectral intensity distribution images of different spectra components. It is the utilization of linear combination of the spectral components using the basis analysis algorithm via eq 1

$$\vec{S_i} = \hat{B}\vec{H_i} + \vec{E_i} \tag{1}$$

where $\vec{S_i}$—spectrum *i* from the spectral dataset, $\hat{B}$—matrix of basis spectra, $\vec{H_i}$—mixing values of spectrum *i*, and $\vec{E_i}$—error spectrum. The mixing values are fitted using least squares minimization methods following the expression 2

$$(\vec{S_i} - \hat{B}\vec{H_i})^2 = \text{minimum}. \tag{2}$$

■ REAGENTS AND SOLUTIONS

Stock solution of ammonium (1.0 g/L), magnesium (1.0 g/L), and phosphate (1.0 g/L) were prepared from monoammonium phosphate, NH$_4$H$_2$PO$_4$ (99.9%+, Fisher Scientific) and MgCl$_2$ (99.9%+, Fisher Scientific). Appropriate amounts of individual salts were weighted into a volumetric flask (100 mL) and dissolved in deionized (DI) water. Working standard solution of ammonium, magnesium, and phosphate were prepared by measuring the appropriate volume of standard solutions into a 100 mL volumetric flask, which was afterwards filled with DI water. Working eluent solutions were prepared by appropriate dilution of standard eluent solution with DI water. An 18.2 MΩ/cm DI water (Millipore, Bedford, MA, USA) was used for dilution in all cases.

MgCO$_3$, CaCO$_3$, CaCl$_2$, Mg(OH)$_2$, and Ca(OH)$_2$ powders (99%+) were obtained from Sigma-Aldrich and used as received.

MgCO$_3$ Reactive Experiments to Form Struvite. All reactions were performed using MgCO$_3$ (Brunauer−Emmett−Teller surface area 94 m^2/g) as the magnesium source. Simulated NH$_4^+$- and PO$_4^{3-}$-containing aqueous solution was prepared by adding 600 ppm of NH$_4$H$_2$PO$_4$ (Fisher Scientific, Certified A.C.S.) at room temperature with constant stirring at 350 rpm, which resulted in a solution with pH of ∼5.4. Concentrations between 300 and 1500 ppm of MgCO$_3$ were added to the aqueous solution containing NH$_4^+$ and PO$_4^{3-}$ and stirred for up to 120 min. The total volume of the reactive solution was 500 mL. The solution (1 mL) was sampled periodically and filtered through a 13 mm diameter polyethersulfone (PES) filter (0.22 μm pore size) to remove solid material and analyzed using IC. Unless specified otherwise, the starting pH was 5.4 before the solid MgCO$_3$ was added in all cases.

Detailed experiments, for example, 300, 1000, and 1500 ppm MgCO$_3$ and 600 ppm NH$_4$H$_2$PO$_4$ used in this work correspond to molar [Mg^{2+}]/[NH$_4^+$]/[PO$_4^{3-}$] ratios of: [0.7:1:1], [2.3:1:1], and [3.4:1:1], respectively. [Mg^{2+}/NH$_4^+$/PO$_4^{3-}$] ratios of [0.5−1.5:1:1] have previously been tested, and it was concluded that lower ratios lead to a lesser N,

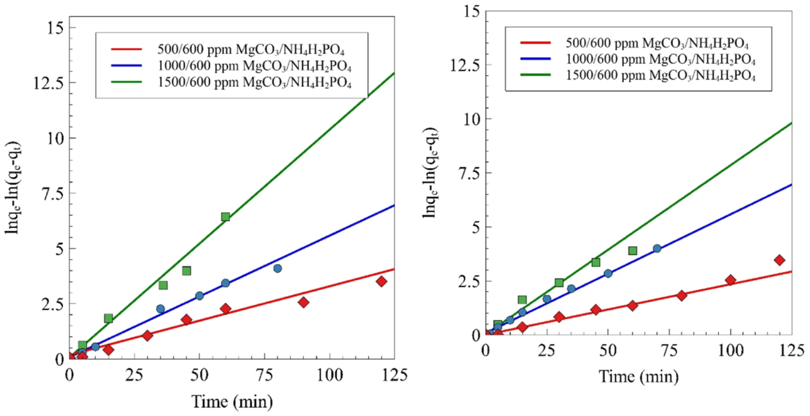

Figure 2. Kinetic modeling of experimental data using pseudo-first-order kinetics model for different starting concentrations of $MgCO_3$. (Left) Total PO_4^{3-} and (right) total NH_4^+.

P, and chemical oxygen demand removal.[32,36−38] A 600 ppm $NH_4H_2PO_4$ represents PO_4^{3-} and NH_4^+ values found in municipal, animal, and industrial wastewater[39] while maintaining the molar 1:1 ion ratio needed for struvite formation. Therefore, a slight excess of Mg^{2+} was preferred in the previous works to circumvent this issue and ensure efficient precipitation of N and P from the solution.[38,40] Further, $CaCl_2$ or $CaCO_3$ were introduced with 1000/600 ppm $MgCO_3/NH_4H_2PO_4$ using molar ratio of Ca^{2+}/Mg^{2+} 1 and 0.2 to assess the change in the final solid product chemical speciation.

NH_4^+ and PO_4^{3-} Adsorption Kinetics. Pseudo-first-order[41,42] kinetic models were used to analyze the obtained NH_4^+ and PO_4^{3-} adsorption data according to the pseudo-first-order model, summarized in eq 3.

$$\ln[q_e - q_t] = \ln q_e - k_1 t \tag{3}$$

where q_t (mg g^{-1}) and q_e (mg g^{-1}) are the amounts of NH_4^+ or PO_4^{3-} adsorbed at time, t (min) and at equilibrium, respectively, whereas k_1 (min^{-1}) is the rate constant of pseudo-first-order kinetic models. Equation 3 can be rearranged to make it suitable for a linear plot as follows.

$$\ln q_e - \ln[q_e - q_t] = k_1 t \tag{4}$$

where the right hand side of the equation is y, and k_1 is the slope.

■ RESULTS AND DISCUSSION

Kinetic Studies of Aqueous $NH_4H_2PO_4$ Reaction with $MgCO_3$. IC was used to monitor the time-dependent anion (PO_4^{3-}) and cation (NH_4^+ and Mg^{2+}) concentration change taking place in the liquid phase during the formation of solid products. Figure 1a shows the concentration profile of residual PO_4^{3-} ions with three different initial $MgCO_3$ concentrations of 300, 1000, 1500 ppm $MgCO_3$ and 600 ppm $NH_4H_2PO_4$ corresponding to molar $[Mg^{2+}]/[NH_4^+]/[PO_4^{3-}]$ ratios of: [∼0.7:1:1], [2.2:1:1], and [3.3:1:1], respectively. These were chosen after testing a wide range of initial $MgCO_3$ concentrations as shown in Figure 1a,c insets. The concentration profiles of the PO_4^{3-} anion showed steep decrease in the cases of 1000 and 1500 ppm $MgCO_3$, but no change was observed using 300 ppm $MgCO_3$. Based on poor ion removal with 300 ppm $MgCO_3$, all subsequent work was performed using 500, 1000, and 1500 ppm $MgCO_3$ with 600 ppm $NH_4H_2PO_4$ corresponding to molar $[Mg^{2+}]/[NH_4^+]/[PO_4^{3-}]$ ratios of: [∼1.1:1:1], [2.2:1:1], and [3.3:1:1], respectively. The highest concentration of $MgCO_3$ exhibited the fastest rate of PO_4^{3-} removal from the solution, with the PO_4^{3-} concentration of 40 ppm at the equilibrium, after 2 h. Concentration profiles of Mg^{2+} in solution as a function of reaction time in Figure 1b showed that there was an immediate dissolution (mobilization) of Mg^{2+} ions from solid $MgCO_3$ within 5 min of the reaction for all $MgCO_3$ concentrations. Equilibrium was achieved rather fast for the unreactive case of 300/600 ppm $MgCO_3/NH_4H_2PO_4$. 1000/600 and 1500/600 ppm $MgCO_3/NH_4H_2PO_4$ experienced a very fast initial dissolution followed by slight decrease in the aqueous Mg^{2+} concentration between 10 and 25 min. The initial fast dissolution was associated with the undersaturated conditions when solid phases, such as struvite, could not form. It was followed by the rapid solid product precipitation accompanied by the corresponding Mg^{2+} concentration decrease. After the solid product formation was complete (similar with the literature reports of fast struvite precipitation within 5−10 min under similar conditions for MgO particles),[16,35] increase in Mg^{2+} concentration was observed to achieve equilibrium after around 2 h of reaction. Time-resolved plot of NH_4^+ adsorption/reaction is shown in Figure 1c, with the inset summarizing removal as a function of $MgCO_3$ concentration. NH_4^+ adsorption and reaction with $MgCO_3$ followed a very similar behavior as that of PO_4^{3-} with undersaturated solution of 300/600 ppm $MgCO_3/NH_4H_2PO_4$ not forming any solid products and higher concentrations resulting in ∼80% NH_4^+ removal from solution. This suggests a facile formation of solids, in contrast to a recent report, where at comparable conditions using MgO, struvite formation only took place under two MgO concentration regimes[16] that is at $[Mg/NH_4^+/PO_4^{3-}]$ molar ratios of 1.4:1:1 (300 ppm MgO) and 4.8:1:1 (1000 ppm MgO). In the case of 300 ppm MgO, maximum removal of NH_4^+ (80%) was achieved at equilibrium after 120 min, whereas in the case of 1000 ppm MgO, a very fast kinetic regime was observed 5 min after the reaction onset to achieve ∼70% removal of NH_4^+.[16] Increase in the initial $MgCO_3$ concentration agreed well with the increasing pH of the solution shown in Figure 1d. Here, the initial 600 $NH_4H_2PO_4$ solution pH was 5.4, and the first measurement with $MgCO_3$ added was taken 1−2 min after the addition. Results show that although pH increased in all three cases, 300 ppm $MgCO_3$ had only gradual change from 6.4 to 7.2 pH units over a the total time of 125 min, whereas 1000 and 1500 ppm $MgCO_3$ exhibited an increase to 8.3 and 8.7, respectively.

To further evaluate the observed kinetics, the NH_4^+ and PO_4^{3-} decrease in concentration shown in Figure 1 was fitted to both pseudo-first-[41,42] and pseudo-second-[16,20,43] (not shown here) order kinetics. The pseudo-first-order plot of ln $q_e - \ln(q_e - q_t)$ versus t, as shown in Figure 2 and summarized in Table 1, fit the experimental data better than pseudo-second-order kinetics, which we reported for struvite formation using MgO.[16] This interesting observation suggests that no complex intermediate is formed in the overall reaction, for example, NH_4^+ and PO_4^{3-} adsorption on $MgCO_3$ is facile and not diffusion limited. This is different from PO_4^{3-} adsorption on MgO where a pseudo-second-order kinetics was measured. Pseudo-second-order kinetics are usually associated with chemisorption mechanism being the rate-controlling step.[44] This is consistent with the previous literature reports where at pH ≈ 7, the rate-controlling step of MgO was a diffusion-limitation process due to protons with the rate proportional to the proton concentration.[45] At pH > 7, the rate-controlling factors were Mg^{2+} and OH^-. These processes as a part of the overall dissolution reaction would lead to the increase in pH observed in this work. $Mg(OH)_2$ forms preferentially at the MgO surface, so that an MgO lattice reaction can be excluded. The increase in pH was rather small, as shown in Figure 1d, in agreement with the absence of the first hydroxylation step leading to a facile pseudo-first-order reaction. From the k_1 values reported in Table 1. it can be seen that the change in k_1

Table 1. Summarized Data from Pseudo-First-Order Kinetic Fits, Shown in Figure 2

	$MgCO_3$ (ppm)	k_1	r^2
PO_4^{3-}	500	0.029	0.97
	1000	0.053	0.99
	1500	0.099	0.98
NH_4^+	500	0.027	0.98
	1000	0.056	0.99
	1500	0.065	0.97

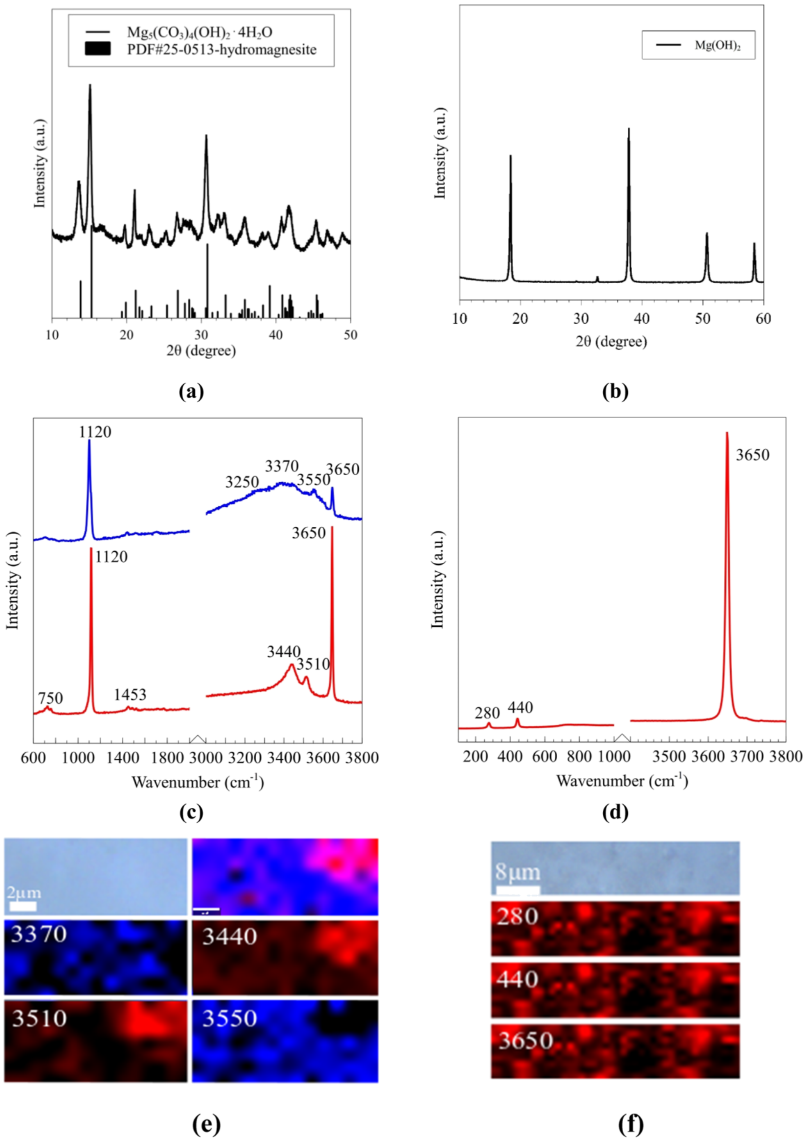

Figure 3. (a) $MgCO_3$ and (b) $Mg(OH)_2$ pXRD spectra. The corresponding Raman spectral components derived from TCA are shown in (c,d), whereas the component individual peak $x-y$ plane maps are shown in (e,f).

DOI: 10.1021/acs.jpcc.8b12252
J. Phys. Chem. C 2019, 123, 8908–8922

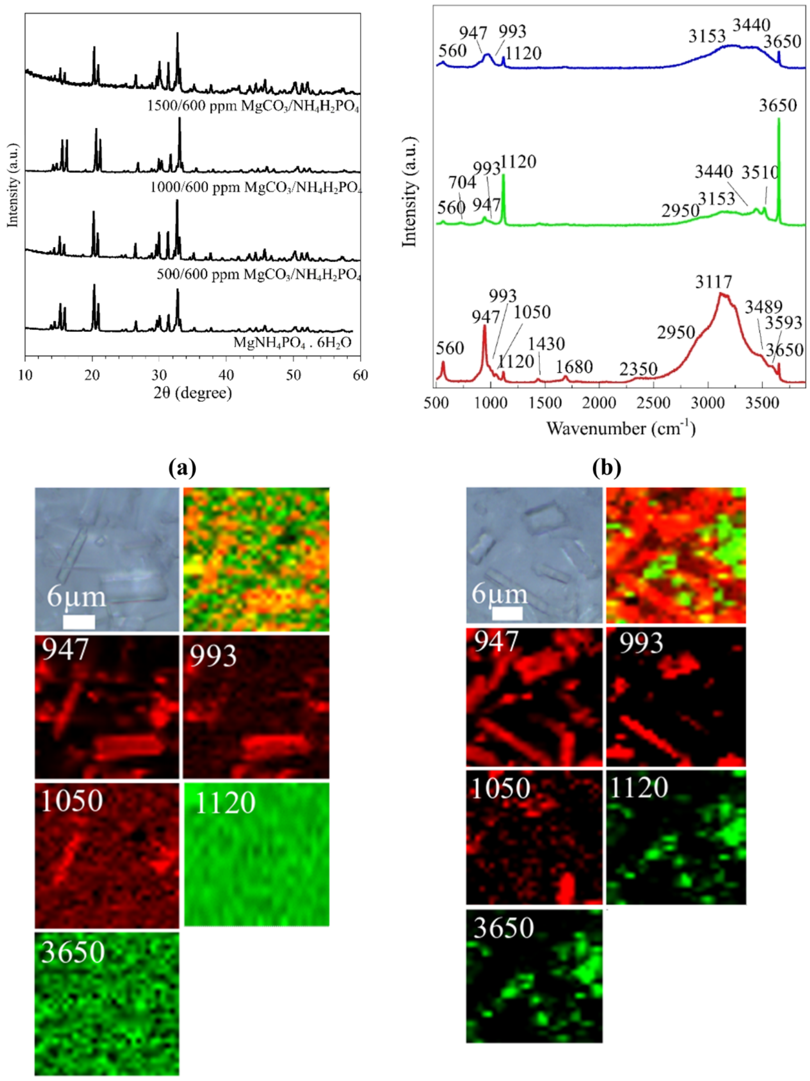

(a) (b)

(c) (d)

Figure 4. (a) pXRD patterns of solid product obtained from 500, 1000, and 1500 ppm $MgCO_3$ with 600 ppm $NH_4H_2PO_4$ after 2 h of reaction, along with reference pXRD of $MgNH_4PO_4{\cdot}6H_2O$ (b) Corresponding Raman spectral components derived from TCA, unique for all experiments described in (a) are shown in (b). The individual peak $x-y$ plane maps are shown in (c) for 500/600 ppm $MgCO_3/NH_4H_2PO_4$ and (d) for 1500/600 ppm $MgCO_3/NH_4H_2PO_4$, both after 2 h of reaction, with starting pH of 5.4.

closely follows the change in the $MgCO_3$ concentration, where doubling the concentration, roughly doubles the rate of PO_4^{3-} and NH_4^+ removal, except in the case of 1500 ppm $MgCO_3$ for NH_4^+ removal.

Compositional and Spatial Homogeneity of the Reactant Magnesium Minerals: $MgCO_3$ and $Mg(OH)_2$. In order to better understand spectral patterns of the reaction products, ex situ Raman experiments combined with pXRD measurements were utilized to better understand compositional complexity of $MgCO_3$ and $Mg(OH)_2$ solid crystals. These data are shown in Figure 3. Chemical complexity of bulk $MgCO_3$ is already apparent from the pXRD pattern shown in Figure 3a. It constitutes a complex hydromagnesite, $4MgCO_3{\cdot}Mg(OH)_2{\cdot}4H_2O$, structure[46] (ICDD-JCPDS PDF#25-0513). Figure 3b shows a well-defined crystalline pattern of $Mg(OH)_2$. Figure 3c shows spectral components obtained using TCA of $MgCO_3$ Raman spectra. The blue component spectrum exhibits a major sharp band at 1120 cm^{-1} and a broad, less intense band with shoulders at 3250, 3370, and 3550 cm^{-1} that correspond to the ν_1 symmetric vibrations of CO_3^{2-} and vibrations of the surface H_2O, respectively. The blue component spectrum also exhibits a sharp band at 3650 cm^{-1} which arises from the surface Mg−OH vibrations.[47] On the other hand, the red component spectrum exhibits peaks at 750, 1120, 1453, 3340, 3510, and 3650 cm^{-1}. According to the literature, all of the red component peaks match those of dypingite, which is another complex hydroxycarbonate species ($Mg_5(CO_3)_4(OH)_2{\cdot}5H_2O$).[47,48] Specifically, 750, 1120, and 1453 cm^{-1} bands are attributed to the ν_2 in-plane bending, the ν_1 symmetric stretching mode, and the ν_3 antisymmetric stretching vibrations of CO_3^{2-} in dypingite, respectively.[47] The overlapping broad bands from 3200 to 3600 cm^{-1} arise from the surface H_2O vibrations, whereas the very sharp band at 3650 cm^{-1} arises from the Mg−OH vibration.[47−49] Hydromagnesite peaks are sharper showing higher degree of crystalline order in agreement with Figure 3a pXRD pattern, where separate dypingite component is not immediately apparent. The corresponding spectral images of the unique

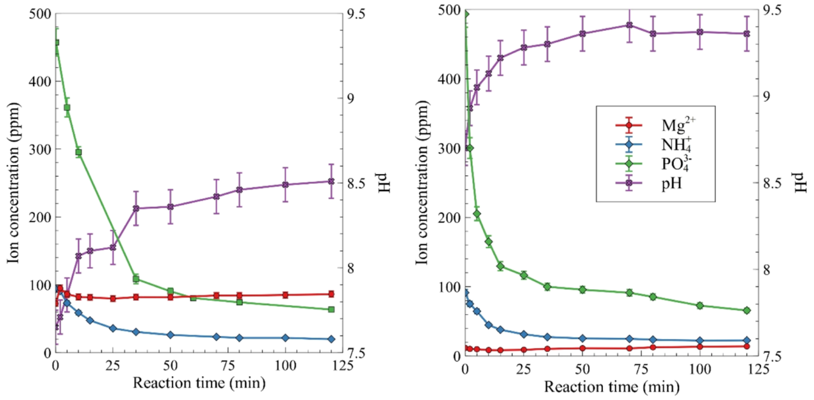

(a) (b)

Figure 5. (a) 1000/600 $MgCO_3/NH_4H_2PO_4$ at starting pH of 5.4. (b) 1000/600 $MgCO_3/NH_4H_2PO_4$ at starting pH of 8.5.

peaks of each component are shown in Figure 3e. Although the optical image appears homogeneous, spatial inhomogeneity becomes apparent in the combined image. Figure 3d shows the only spectral component obtained using TCA of $Mg(OH)_2$ Raman scan. The 280, 440, and 3650 cm^{-1} bands agree well with the literature and are attributed to lattice vibrations that are perpendicular ($E_g(T)$) or parallel ($A_{1g}(T)$) to the crystal *c*-axis and symmetric OH stretching vibrations, respectively.[50,51] The 3650 cm^{-1} peak assignment in hydromagnesite (Figure 3c) is thus corroborated by the $Mg(OH)_2$ spectrum. Spectral mapping of $Mg(OH)_2$ shown in Figure 3f confirms the presence of a single spectral component with some discontinuities in the image because of the shallow depth of field.

Compositional and Spatial Homogeneity of Struvite Crystals Formed via NH_4^+ and PO_4^{3-} Adsorption/Reaction on $MgCO_3$. Next, the effect of $MgCO_3$ concentration on the solid product speciation and homogeneity was probed via pXRD and Raman. The starting pH was 5.4 (that of 600 ppm $NH_4H_2PO_4$) in this round of analysis. Three concentrations of $MgCO_3$, that is 500, 1000, and 1500 ppm, were utilized, whereas 600 ppm $NH_4H_2PO_4$ was used in all cases. 500, 1000, and 1500 ppm $MgCO_3$/600 ppm $NH_4H_2PO_4$ correspond to molar ratios of [$Mg^{2+}/NH_4^+/PO_4^{3-}$] of [1.1:1:1], [2.2:1:1], and [3.3:1:1], respectively. These ratios were chosen to represent three concentration regimes: Mg-stoichiometric, Mg-rich, and Mg-excess. pXRD results shown in Figure 4a clearly show that in all three cases the solid product bulk crystalline structure was the same and matched that of struvite.[16,35] To analyze the identity and molecular structures present at the solid product surface in a spatially resolved manner, 500/600 ppm $MgCO_3/NH_4H_2PO_4$ and 1500/600 ppm $MgCO_3/NH_4H_2PO_4$ were further analyzed with Raman spectroscopy, and major spectral components were identified using TCA. For all spectra in Figure 4b, the data showed three unique spectral components present. Literature data showed that struvite crystals synthesized using aqueous 1:1 NH_4^+ and PO_4^{3-} solutions and water soluble $MgCl_2$ exhibited Raman bands at 101, 144, 189, 229, 297, 393, 440, 570, 700, 750, 950, 981, 1020, 1125, 1429, 1469, 1675, 2357, a broad band at 2800−3430, 3498, and 3603 cm^{-1}.[35] The bands from 101 through 570 cm^{-1} were attributed to the skeletal vibrations of struvite.[35,49] A sharp, prominent band at ~950 cm^{-1} and smaller bands at 981 and 1020 cm^{-1} were attributed to the symmetric and asymmetric PO_4^{3-} stretches, respectively.[35] Two prominent peaks in 1400−1700 cm^{-1} region were assigned to the deformational vibrations of NH_4^+ tetrahedra.[52] Lastly, a broad band corresponding to different N−H and O−H (in H_2O) stretches was observed in the 2200−3600 cm^{-1} region because of the hydrogen bonding. The red component in Figure 4b was assigned to struvite. The green component with major bands at 1120, 3440, 3510, and 3650 cm^{-1} and minor shoulders at 560, 704, 947, 993, 2950, and 3153 cm^{-1} can be interpreted as a magnesium-rich dypingite-like phase.[47] Any surface OH groups will exhibit a sharp band at ~3650 cm^{-1} due to the symmetric Mg−OH stretch. Hence, the blue component exhibited major bands at 560, 947, 993, 1120, 3153, 3440, and 3650 cm^{-1}. Based on band assignments in Figure 3c, which shows characterization data of the reactant precursor, it can be concluded that this is an intermediate to struvite with $MgCO_3$-like chemical environment and few OH groups on the surface. Based on these TCA components shown in Figure 4b, Raman maps for 500/600 ppm $MgCO_3/NH_4H_2PO_4$ and 1500/600 ppm $MgCO_3/NH_4H_2PO_4$ were constructed and shown in Figure 4c,d, respectively. Only unique peaks of each component were utilized to analyze localization of different solid phases. In both cases, the red component with bands at 947, 993, and 1050 cm^{-1} was predominantly present in the highest intensity within the crystalline needles, which is the predominant crystal shape of struvite.[35] The solid product surrounding the crystalline needles showed localization of the green component, with Raman bands at 1120 and 3650 cm^{-1} from CO_3^{2-} and OH^- species, respectively. Very little of the blue component was present in the spectral images. It is key to note that in the case of 1500/600 ppm $MgCO_3/NH_4H_2PO_4$, much less green component was present in Raman maps compared to those of 500/600 ppm $MgCO_3/NH_4H_2PO_4$, suggesting that a large excess of $MgCO_3$ is needed to consume this intermediate phase and push the equilibrium toward struvite formation.

Effect of Initial pH on Spatial Distribution and Speciation of the Solid Products. Surface water pH can range anywhere from 6.0 to 9.0.[53] Additionally, pH of certain wastewaters, such as wastewater from the swine industry (or even municipal wastewater) have pH values above 8.[38] The equilibrium pH of the aqueous PO_4^{3-} and NH_4^+ at 600 ppm without any extraneous ions present would yield a pH value of ~5.4, which increased to 8.5 upon reaction because of the release of OH^- ions. Higher initial pH of 8.5 was achieved by adjusting it with NaOH, and the reaction was repeated with 1000 ppm $MgCO_3$. The results are shown in Figure 5b compared to those with the initial pH of 5.4 (Figure 5a). Adsorption/reaction of PO_4^{3-} and NH_4^+ proceeded with faster initial kinetics, for example, a steeper decrease in the aqueous ion concentration was observed than in Figure 5a. The corresponding initial decrease rates were found using linear fit and were 2 and 4 ppm/min for NH_4^+ and 8.4 and 15 ppm/min for PO_4^{3-} for the initial pH of 5.4 and 8.5*m*, respectively. This is consistent with the literature data, where increasing pH facilitated struvite formation.[38] More importantly, virtually no Mg^{2+} ions were detected during the experiments in solution with starting pH of 8.5, as most of Mg^{2+} is transformed into low-solubility compounds, such as $Mg(OH)_2$ ($K_{sp} = 5.1 \times 10^{-12}$) and Mg_3PO_4 ($K_{sp} = 1.0 \times 10^{-24}$).[54] This suggests a pH-specific reaction mechanism, where initial pH can alter the amount of Mg^{2+} available. For example, a significant fraction of Mg^{2+} ions ~80% for 1000, as shown in Figures 5a and 1b, is still present in aqueous solution and needs to diffuse to the surface to achieve super saturation toward struvite formation. However, when initial pH of 8.5 was used at 1000 ppm $MgCO_3$, almost no Mg^{2+} remained in the solution (Figure 5b).

Unique peaks from TCA components shown in Figure 4b were used to construct Raman maps. The resulting spectral map images are shown in Figure 6. In both cases (initial pH 5.4 and 8.5), the major crystalline product was needles of struvite, red TCA component, whereas the amorphous particles exhibited bands present in the green TCA component. Both cases showed similar component distribution with green and red present in comparable amounts. Based on a similar spatial distribution of each component, it can be proposed that struvite synthesis using very low-solubility $MgCO_3$ precursor does not show a distinct pH dependence on the solid products speciation at the equilibrium in the pH range tested. In contrast, a strong pH effect on solid product distribution was previously shown[16] during struvite synthesis using MgO, where the initial pH of 8.5 led to PO_4^{3-} consumption decreasing significantly and yielded solid $Mg_3PO_4{\cdot}22H_2O$ and unreacted MgO with virtually no struvite after 120 min of reaction time. On the other hand, when the synthesis solution was buffered at the pH of 9.2, pXRD analysis of the solid products showed a mixture of struvite and $Mg_3PO_4{\cdot}22H_2O$. No solid MgO phase was observed after 120 min synthesis.[16] When $MgCO_3$ was used, no such pH dependence was observed. This is because in the case of MgO precursor, a slow dissolution step to form surface OH species is necessary, which depends not only on temperature, defect density, particle size, but also, on pH of the solution.[45,55−57] However, in the case of $MgCO_3$, the surface already has abundant OH groups present, as shown by the 3650 cm^{-1} band in Figure 3. Presence of OH^--truncated surface implies that the dissolution step in this case is not as slow, but more importantly, its pH dependence is absent[58,59] in the pH range of 5.4−8.5, which is used in this work.

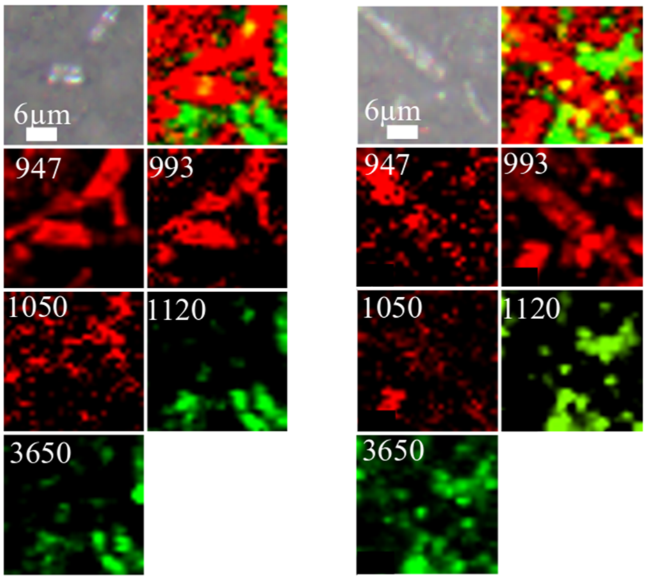

(a) (b)

Figure 6. The unique Raman band maps are shown in (a) for 1000/600 ppm $MgCO_3/NH_4H_2PO_4$ with initial pH of 5.4 and (b) for 1000/600 ppm $MgCO_3/NH_4H_2PO_4$ with initial pH of 8.5, as adjusted with NaOH, both after 2 h of reaction. Unique Raman bands were inferred from total component analysis shown in Figure 4b, as the components do not change because the identity of chemical species is the same, but the relative intensity of the unique Raman bands changes.

Effect of Ca^{2+} from Low-Solubility $CaCO_3$ on Solid Product Speciation. Numerous studies reported in the literature show inhibitory effect of Ca^{2+} ions during struvite synthesis.[60−64] In particular, presence of Ca^{2+} ions in solutions containing NH_4^+, PO_4^{3-} and Mg^{2+} ions leads to competitive reactions between struvite formation using Mg^{2+} ions and calcium phosphate formation using Ca^{2+} ions.[60−64] As the Ca^{2+}/Mg^{2+} ratio in the solution increases, the thermodynamically dominant product becomes calcium phosphate.[14] However, little information is available where $NH_4^+$and PO_4^{3-} solutions are exposed to solid low-solubility Ca^{2+} precursors, such as $CaCO_3$, as most studies employed soluble $MgCl_2$ and $CaCl_2$. This is especially important in the environment where dolomite, a solid solution of $CaCO_3$ and $MgCO_3$, is present as a natural mineral.[65]

Solid $CaCO_3$ particles were first characterized using pXRD and Raman spectroscopy, as shown in Figure 7. pXRD analysis in Figure 7a showed a complete agreement of pXRD peaks with the literature reports of crystalline $CaCO_3$ phase.[66,67] The Raman spectrum shown in Figure 7c exhibited major bands at 280, 705, 1086, and 1434 cm^{-1}, which are attributed to the lattice mode, ν_4 in-plane bending, ν_1 symmetric stretch, and ν_3 antisymmetric stretch of the CO_3^{2-}, respectively.[66,68,69] TCA showed only a single spectral component. Spectral maps of the representative peaks shown in Figure 7d clearly showed the spectral component present homogenously throughout the sample, with the three bands (280, 705, and 1086 cm^{-1}) showing intensity at the same locations. $Ca(OH)_2$, a potential reactive intermediate of $CaCO_3$ hydration was also analyzed as shown in Figure 7b,d,f. The pXRD pattern agreed well with the literature.[70] Likewise, Raman analysis showed only a single spectral component with major bands at 350 and 684 cm^{-1} attributed to vibrations of Ca−O and the 3615 cm^{-1} OH stretch.[71,72] A small shoulder at 1086 cm^{-1} was inferred from Figure 7c as $CaCO_3$ impurity and has been observed in other studies.[72]

Having established spectral properties of $CaCO_3$ and $Ca(OH)_2$, two Ca^{2+}/Mg^{2+} ratios, namely, 0.2 and 1 were chosen for reactions with aqueous NH_4^+ and PO_4^{3-}, whereas $MgCO_3$ and $NH_4H_2PO_4$ concentrations of 1000/600 ppm remained the same. This resulted in precursor concentrations of 1000/600/238 ppm and 1000/600/1190 ppm of $MgCO_3$/

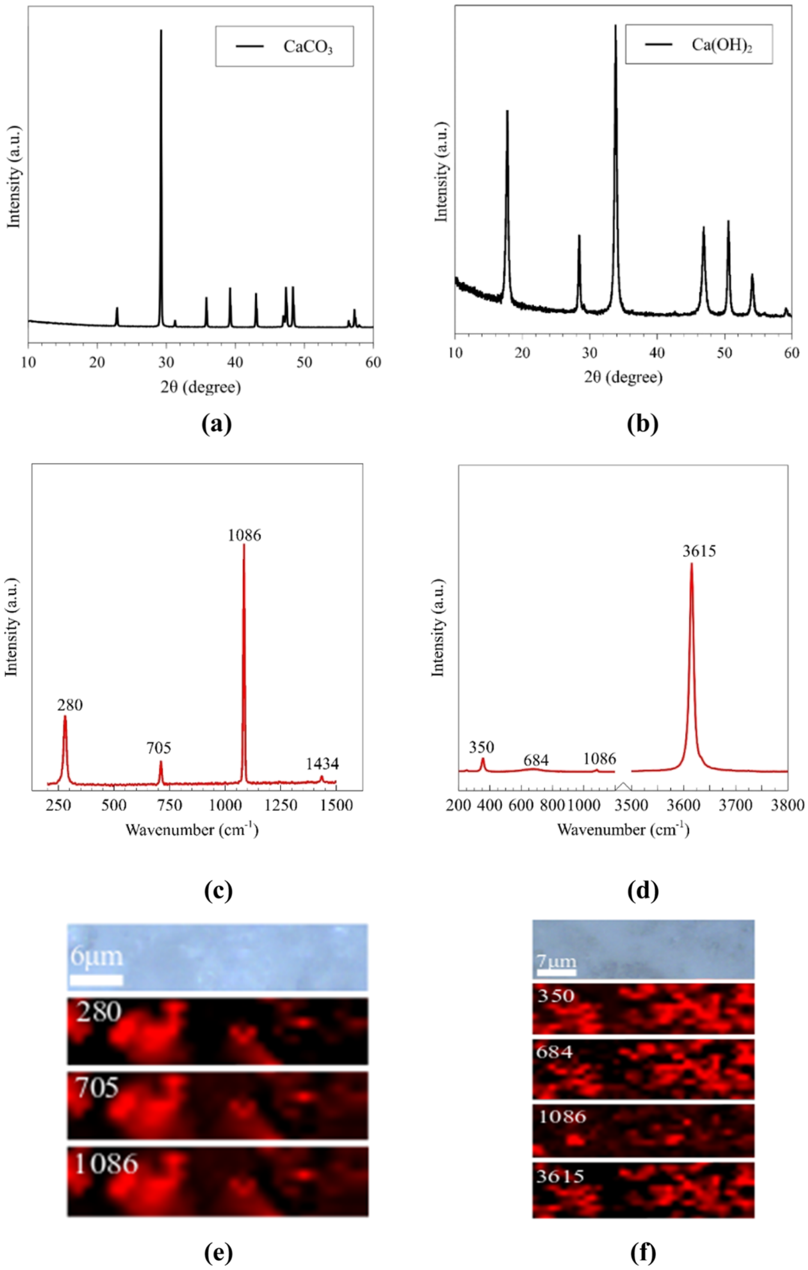

(a) (b) (c) (d) (e) (f)

Figure 7. (a) $CaCO_3$ and (b) $Ca(OH)_2$ pXRD spectra. The corresponding Raman spectral components derived from TCA are shown in (c,d), whereas the component individual peak $x-y$ plane maps are shown in (e,f).

$NH_4H_2PO_4/CaCO_3$, respectively. The solid products formed were analyzed using pXRD and Raman spectroscopy, as shown in Figure 8. pXRD analysis in Figure 8a unequivocally showed that at both ratios tested, struvite was the dominant product. However, in the case of $Ca^{2+}/Mg^{2+} = 1$, an unreacted CO_3^{2-} phase was also observed in the product, as seen from the CO_3^{2-} peak in Figure 8a Raman TCA results shown in Figure 8b resulted in three unique spectral components. Based on Raman assignments made above (Figures 3, 4, and 7) and in the literature,[16] the red component bands matched those of struvite, with the exception of 1086 cm^{-1} which corresponded to solid $CaCO_3$. The blue component exhibited major bands at 707, 947, 1086, 1430, and 1680 cm^{-1} that agreed well with those of $CaCO_3$ except for the 947 cm^{-1} band, which is attributed to the PO_3^{3-} vibration, also seen in Raman spectra of struvite (red component). Lastly, the green component exhibited bands similar to those of the red component suggesting struvite. However, the green component exhibited both 1086 and 1120 cm^{-1} bands that correspond to CO_3^{2-} coordinated to both Ca^{2+} and Mg^{2+}, respectively. This suggests complex solid reaction products with the green component corresponding to a struvite phase rich in both $MgCO_3$ and $CaCO_3$, whereas the red component corresponds to a struvite phase rich in $CaCO_3$.

The TCA maps based on the unique bands of each component shown in Figure 8b for Ca^{2+}/Mg^{2+} ratios 0.2 and 1 are shown in Figure 8c,d, respectively. These maps were acquired on a single crystal, as shown in the optical image, in the $x-z$ direction parallel to the laser beam. Effectively, they resulted in the information obtained from the cross-section of a single crystal. In both cases, it can be clearly seen that the red component with notable bands at 947, 993, and 1050 cm^{-1}

DOI: 10.1021/acs.jpcc.8b12252
J. Phys. Chem. C 2019, 123, 8908−8922

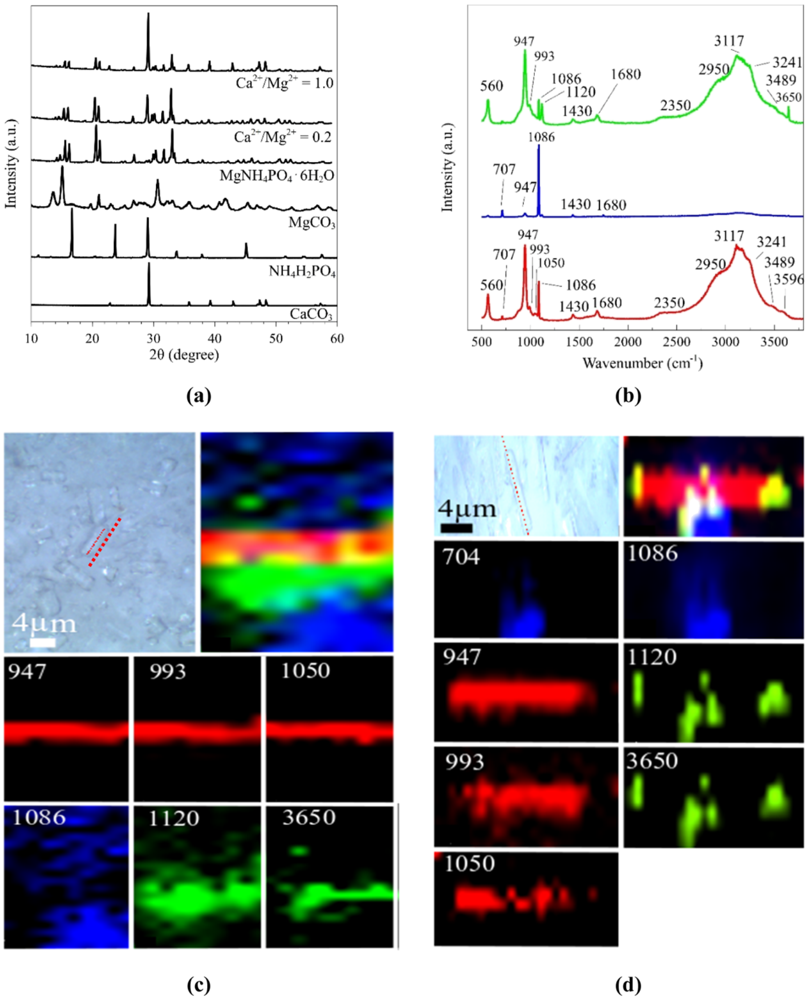

(a)

(b)

(c)

(d)

Figure 8. (a) pXRD patterns of reactants and the reaction products during struvite formation from 1000/600 $MgCO_3/NH_4H_2PO_4$ solutions with and without $CaCO_3$. (b) Raman TCA components of 1000/600 $MgCO_3/NH_4H_2PO_4$ with $CaCO_3$ added into the reaction mixture. (c) Spectral component individual peak $x-z$ plane maps for 1000/600 ppm $MgCO_3/NH_4H_2PO_4$ with $CaCO_3$ and molar ratio of Ca^{2+}/Mg^{2+} = 0.2. (d) Individual peak $x-z$ plane maps for 1000/600 ppm $MgCO_3/NH_4H_2PO_4$ with $CaCO_3$ and molar ratio of Ca^{2+}/Mg^{2+} = 1. Reaction products collected and analyzed after 2 h of reaction. The red dotted line in the optical image represents the path of the laser beam scan. Starting pH in each case was the equilibrium pH of $NH_4H_2PO_4$ solution that is, 5.4.

due to struvite is localized in the crystalline product homogenously. The blue component with the main peak at 1086 cm^{-1} due to $CaCO_3$ is localized outside the crystalline product in the particles, which is likely due to the intermediate reactive species. Lastly, in the Ca^{2+}/Mg^{2+} ratio of 0.2, the green component with unique peaks at 1120 and 3650 cm^{-1} due to $MgCO_3$ is dominantly present outside the crystalline product as part of the particles. For Ca^{2+}/Mg^{2+} ratio of 1, the green component was present within the crystals, especially at their edges. Although a dramatic inhibitory effect of Ca^{2+} on struvite formation was not observed in the current experiments, the presence of unreacted $MgCO_3$ phase (green component) within the crystalline product can tentatively be interpreted as a result of slight retardation of struvite formation with higher Ca^{2+} content present in the solution. The absence of a strong inhibitory effect of Ca^{2+} from $CaCO_3$ was most likely not observed due to slower dissolution of $CaCO_3$ compared to $MgCO_3$, which has been reported in the literature.[58] Slower $CaCO_3$ dissolution led to the excess Mg^{2+} present in the solution facilitating struvite formation.

Spatial resolution of Raman spectroscopy is dependent upon laser wavelength, as well as numerical aperture-limited and is within ~1 μm.[73] Complementary electron microscopy analysis was conducted to attain greater resolution to investigate if calcium ions were indeed incorporated into the struvite crystal structure, as shown in Figure 9. For both Ca^{2+}/Mg^{2+} ratios of 0.2 and 1, it can clearly be seen that green (Mg), teal (O), and orange (P) components exhibit strong intensities and are colocalized, corroborating homogenous struvite structure of the product. Interestingly, red (Ca) was shown to be present in both the samples in island-like formations, as seen in Figure 9b. By using low-solubility $CaCO_3$ as the Ca^{2+} source during struvite formation, Ca^{2+} was incorporated into the struvite structure to effectively form Ca-incorporated struvite.

Effect of Ca^{2+} from High-Solubility $CaCl_2$ on Solid Product Speciation. A strong inhibitory effect of Ca^{2+} on struvite crystal formation was not observed when using low-solubility $CaCO_3$ precursor, at both Ca^{2+}/Mg^{2+} ratios of 0.2 and 1, as shown in Figures 8 and 9. However, inhibitory effect was observed when using soluble $CaCl_2$, especially in the case of Ca^{2+}/Mg^{2+} = 1 (Figure 10). Consistently, two Ca^{2+}/Mg^{2+} ratios, namely 0.2 and 1, were used for reactions with aqueous NH_4^+ and PO_4^{3-}, whereas $MgCO_3$ and $NH_4H_2PO_4$ concentrations remained the same. This resulted in 1000/600/268

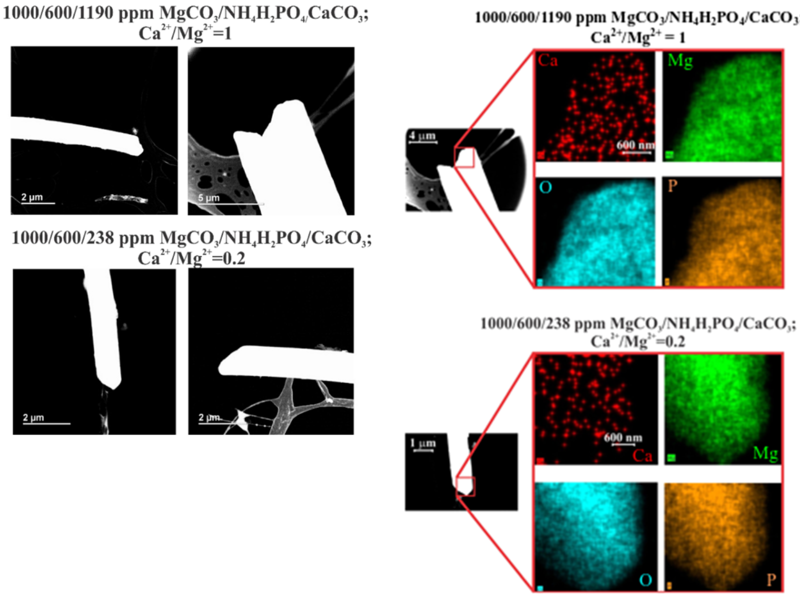
1000/600/1190 ppm $MgCO_3/NH_4H_2PO_4/CaCO_3$; $Ca^{2+}/Mg^{2+}=1$

1000/600/238 ppm $MgCO_3/NH_4H_2PO_4/CaCO_3$; $Ca^{2+}/Mg^{2+}=0.2$

(a)

(b)

Figure 9. (a) STEM images of single struvite crystalline particle for $CaCO_3$ calcium source using Ca^{2+}/Mg^{2+} ratios of 0.2 and 1. (b) Selected area STEM-EDS maps of a single struvite particle. Red—Ca, green—Mg, cyan—O, and orange—P.

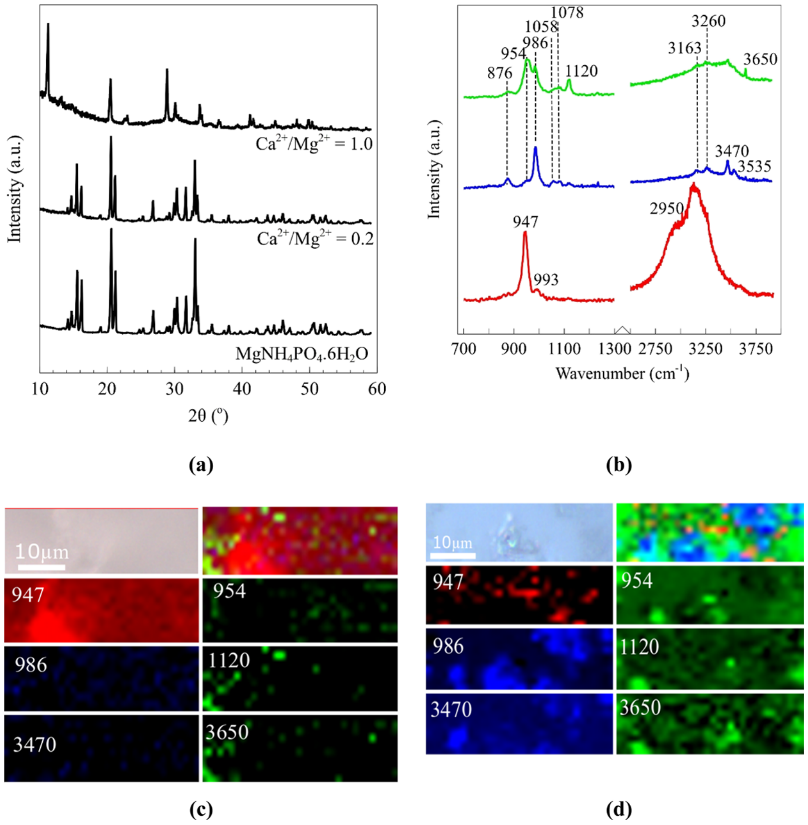

(a)

(b)

(c)

(d)

Figure 10. (a) pXRD patterns of reactants and the reaction products during struvite formation from 1000/600 $MgCO_3/NH_4H_2PO_4$ solutions with and without $CaCl_2$. (b) Raman TCA components of 1000/600 $MgCO_3/NH_4H_2PO_4$ with $CaCl_2$ added into reaction mixture. (c) Spectral component individual peak x−y plane maps for 1000/600 ppm $MgCO_3/NH_4H_2PO_4$ with $CaCl_2$ and molar ratio of Ca^{2+}/Mg^{2+} = 0.2. (d) Spectral component individual peak x−y plane maps for 1000/600 ppm $MgCO_3/NH_4H_2PO_4$ with $CaCl_2$ and molar ratio of Ca^{2+}/Mg^{2+} = 1. Reaction products collected and analyzed after 2 h reaction. Starting pH in each case was the equilibrium pH of 600 ppm $NH_4H_2PO_4$ solution, that is 5.4.

ppm and 1000/600/1340 ppm of $MgCO_3/NH_4H_2PO_4/CaCl_2$, respectively. The solid products were characterized using pXRD and Raman spectroscopy as shown in Figure 10. pXRD analysis showed that at Ca^{2+}/Mg^{2+} ratio of 0.2, struvite was obtained as the major product, whereas in the case of Ca^{2+}/Mg^{2+} ratio of 1, the pXRD pattern did not match that of struvite but, instead, matched that of $CaCl_2$.[74] The latter observation is distinctly different from the data shown in Figure 8, where $CaCO_3$ was utilized but consistent with the literature reports, where soluble precursors were used as Ca^{2+} sources.[60−64] TCA derived from Raman scans showed three unique components shown in Figure 10b. The red spectral component exhibited major bands at 947 and 993 cm^{-1} and a broad band with a shoulder at 2950 cm^{-1}; all assigned to struvite.[16] The blue spectral component exhibited major bands at 876, 986, 1058, 1078, 3163, 3260, 3470, and 3535 cm^{-1}. The bands in 954−1078 and 3163−3535 cm^{-1} ranges originate from distorted PO_4^{3-} and surface OH vibrations, respectively.[75] In fact, calcium phosphate-containing minerals, such as hydroxyapatite, have been shown to exhibit similar bands.[76−79] Lastly, green spectral component exhibited bands at 276, 954, 986, 1058, and 1078 cm^{-1} and a broad band with shoulders at 3163, 3260 and 3650 cm^{-1}. As most of these bands present in the green spectral component are combinations of the bands in red (struvite) and blue (calcium hydroxyphosphate) components, the green component can be regarded as an intermediate to the two products with excess $MgCO_3$ according to 1120 and 3650 cm^{-1} bands. Raman *x*−*y* maps of unique bands of each spectral component, namely, 947 cm^{-1} for struvite, 986 and 3470 cm^{-1} for calcium hydroxyphosphate, and 954, 1120, and 3650 cm^{-1} for the intermediate to struvite and calcium hydroxyphosphate phases, are shown in Figure 10c,d for Ca^{2+}/Mg^{2+} ratio of 0.2 and 1, respectively. For Ca^{2+}/Mg^{2+} of 0.2, the maps show struvite as the dominant product present homogenously throughout the area. However, the lack of the main crystal habit of struvite—needles—[35]ints at poor crystallinity of the struvite formed. No blue spectral component was observed in the product with a few spots of the green spectral component. On the other hand, for Ca^{2+}/Mg^{2+} ratio of 1, very little struvite—red spectral component—can be seen in the solid product. In fact, the dominant solid phase comprised an intermediate $MgCO_3$-rich phase as inferred from the strong intensity of the 1120 and 3650 cm^{-1} bands. The blue spectral component, which corresponds to calcium hydroxyphosphate species—represented by 986 and 3470 cm^{-1} bands—also exhibited strong intensity in the scanned area and was present wherever red and green components were not.

The TCA and peak maps in conjunction with pXRD results showed that introducing calcium via soluble $CaCl_2$ leads to instantaneous availability of Ca^{2+} ions when compared to Mg^{2+} ions as $MgCO_3$ dissolution is significantly slower. This leads to poor crystalline quality of struvite in the case of $Ca^{2+}/Mg^{2+} = 0.2$, and calcium hydroxyphosphate, in the case of Ca/Mg = 1, as the major product. With the instantaneous availability of Ca^{2+} ions, the formation of calcium phosphate starts to compete with struvite formation, which is clearly kinetically hindered due to slower Mg^{2+} release, leading to the strong inhibitory effect of Ca^{2+}, often reported in the literature.[54,60−64]

■ DISCUSSION

A previous work suggested that solid Mg^{2+} precursor above stoichiometric amount is typically needed to form struvite crystals.[31] The fate of the unreacted Mg^{2+} is of major interest because chiefly, pXRD has been utilized to assess the solid reaction product composition,[38] effectively eliminating from consideration any amorphous intermediates or products, such as magnesium hydroxycarbonates that can form via hydromagnesite reactions with water under ambient conditions. pXRD data in this work showed that for all $MgCO_3/NH_4H_2PO_4$ ratios, struvite was the only crystalline product, whereas Raman analysis suggested that a dypingite-like phase was also present. Although the exact phase is difficult to assign from Raman spectrum only, the dypingite phase is expected because a dypingite unit cell is more expanded than hydromagnesite because of higher crystalline water content.[80] Similar equilibrium product was observed in parallel with struvite formation using MgO particles with the reaction following pseudo-second-order kinetics.[16] However, adsorption of PO_4^{3-} ions on hydromagnesite followed pseudo-first-order kinetics suggesting no complex kinetics of hydromagnesite hydration to form a reactive intermediate, in contrast to the MgO case, where the rate-controlling step was OH^- adsorption followed by Mg^{2+} and OH^- desorption. At the time scales used in this study (, maximum reaction time of 120 min), higher hydromagnesite content (1000−1500/600 ppm $MgCO_3/NH_4H_2PO_4$) was needed to form well-defined struvite crystals, whereas lower content—300/600 ppm $MgCO_3/NH_4H_2PO_4$ corresponding to a substoichiometric $[Mg^{2+}/NH_4^+/PO_4^{3-}]$ of [0.7:1:1]—mostly transformed hydromagnesite into higher crystalline water content species.

Moreover, Ca^{2+} source (soluble $CaCl_2$ vs low-solubility $CaCO_3$) had a strong effect on the equilibrium solid product speciation. Formation of crystalline carbonate minerals via an amorphous precursor[81] containing Mg^{2+} ions was shown to be kinetically slow, whereas magnesium-substituted amorphous calcite formation was fast. This phenomenon was attributed to the structural water bound to Mg ions hindering dehydration and transformation into the crystalline state. Accordingly, a distinct phase speciation was observed in both pXRD and Raman spectra when $CaCO_3$ is present, up to Ca^{2+}/Mg^{2+} molar ratio of 1, with a maximum reaction time of 120 min. Unique Raman spectral patterns that encompass both PO_4^{3-} and CO_3^{2-} ion vibrations are likely due to the incorporation of isovalent Ca^{2+} and Mg^{2+} carbonate particle inclusions into the struvite crystals. This is a prevalent mode of solid product crystallization at $Ca^{2+}/Mg^{2+} = 1$, whereas at $Ca^{2+}/Mg^{2+} = 0.2$, calcium-containing solid particles are more diffused. Using soluble $CaCl_2$ at $Ca^{2+}/Mg^{2+} = 0.2$ inhibited the struvite crystal formation to a smaller extent, whereas $Ca^{2+}/Mg^{2+} = 1$ from $CaCl_2$ exhibited strong struvite formation inhibition, producing an entirely different solid product. Again, in the case of $CaCl_2$, the maximum reaction time was 120 min. In the case of $Ca^{2+}/Mg^{2+} = 1$ from $CaCl_2$, calcium hydroxyapatite formation proceeded in parallel to struvite formation, with a unique Raman spectrum that contained CO_3^{2-} ion vibrations. According to the spectral maps, this component was not colocalized with either struvite or hydroxyapatite and can potentially correspond to hydroxyl apatite species, where hydroxyl groups are partially substituted by CO_3^{2-} ions.[82]

To summarize, at the time scale studied, the different reaction products observed spectroscopically during reactive transformation of $MgCO_3$ indicate that struvite crystallization is significantly affected by the composition of the reactive environment, including $MgCO_3/NH_4H_2PO_4$ ratio, Ca^{2+}/Mg^{2+} ratio, and the solubility of the calcium precursor.

■ CONCLUSIONS

Our results present spectral evidence of different transformation products of $MgCO_3$ particles—in the form of hydromagnesite—in NH_4^+- and PO_4^{3-}-containing aqueous solutions, with and without Ca^{2+} ions present. The formation of the crystalline phase struvite was observed using pXRD in predominant number of solution compositions except when $CaCl_2$ at Ca^{2+}/Mg^{2+} = 1 was used, with all studies at a maximum reaction time of 120 min. Ex situ Raman spectra, however, provided much deeper understanding of the low crystallinity solid materials not identified via bulk X-ray analysis. For $MgCO_3$ concentrations where sufficient supersaturation resulted in significant precipitation of both NH_4^+ and PO_4^{3-} ($MgCO_3$ > 500 ppm; $NH_4H_2PO_4$ = 600 ppm; $[Mg^{2+}/NH_4^+/PO_4^{3-}]$ = 1.1:1:1), formation of solid struvite was accompanied by a dypingite-like phase formation due to the extra water molecule incorporation into the crystalline structure of the hydromagnesite. Single crystal Raman and STEM/EDXS studies showed complex solid materials formed with Ca^{2+} substituting into the structure of struvite crystals as submicron crystallites. These crystallites possess functional groups of PO_4^{3-} and CO_3^{2-} from both $MgCO_3$ and $CaCO_3$. A distinct difference in solid product speciation was observed when $CaCl_2$ was used as the calcium source. Crystallinity of the struvite product significantly decreased when Ca^{2+}/Mg^{2+} = 0.2 was used, whereas a distinct shift toward calcium hydroxyapatite was observed for Ca^{2+}/Mg^{2+} = 1. These observations clearly highlight the importance of the physicochemical parameters, such as concentration of $MgCO_3$, pH, Ca^{2+} ion concentration, and the solubility of their source on the formation of a distinct crystalline struvite phase. Results presented herein have implications for nutrient (N and P) recovery and recycling from wastewater streams in the form of sustainable, slow-release fertilizers utilizing insoluble and abundant magnesium minerals.

■ AUTHOR INFORMATION

Corresponding Author

*E-mail: job314@lehigh.edu. Phone +1-610-758-6836.

ORCID

Jonas Baltrusaitis: 0000-0001-5634-955X

Author Contributions

B.L. and D.K. contributed equally. B.L. performed struvite growth and IC studies, W.T. performed struvite growth at different Ca^{2+}/Mg^{2+} precursor ratio, D.B. and D.K. performed Raman analysis, K.H. performed pXRD studies, and L.Z. performed STEM measurements. Lastly, J.B. & D.K. performed experimental design, data analysis, and wrote the manuscript.

Notes

The authors declare no competing financial interest.

■ ACKNOWLEDGMENTS

This material is based upon work supported by the National Science Foundation under grant no. CHE 1710120. This research used Hitachi 2700C STEM of the Center for Functional Nanomaterials, which is a U.S. DOE Office of Science Facility, at Brookhaven National Laboratory under contract no. DE-SC0012704. We acknowledge the help of Yiying Sheng for assistance with IC experiments.

■ REFERENCES

(1) Bouwman, L.; Goldewijk, K. K.; Van Der Hoek, K. W.; Beusen, A. H. W.; Van Vuuren, D. P.; Willems, J.; Rufino, M. C.; Stehfest, E. Exploring global changes in nitrogen and phosphorus cycles in agriculture induced by livestock production over the 1900-2050 period. *Proc. Natl. Acad. Sci. U.S.A.* **2013**, *110*, 20882−20887.

(2) Baltrusaitis, J. Sustainable Ammonia Production. *ACS Sustainable Chem. Eng.* **2017**, *5*, 9527.

(3) Patil, B. S.; Wang, Q.; Hessel, V.; Lang, J. Plasma N_2-fixation: 1900-2014. *Catal. Today* **2015**, *256*, 49−66.

(4) Galloway, J. N.; Aber, J. D.; Erisman, J. W.; Seitzinger, S. P.; Howarth, R. W.; Cowling, E. B.; Cosby, B. J. The Nitrogen Cascade. *Bioscience* **2003**, *53*, 341−356.

(5) Galloway, J. N.; Cowling, E. B. Reactive Nitrogen and The World: 200 Years of Change. *AMBIO A J. Hum. Environ.* **2002**, *31*, 64−71.

(6) Wang, H.; Wang, H. Mitigation of Lake Eutrophication: Loosen Nitrogen Control and Focus on Phosphorus Abatement. *Prog. Nat. Sci.* **2009**, *19*, 1445−1451.

(7) Canfield, D. E.; Glazer, A. N.; Falkowski, P. G. The Evolution and Future of Earth's Nitrogen Cycle. *Science* **2010**, *330*, 192−196.

(8) Cameron, K. C.; Di, H. J.; Moir, J. L. Nitrogen Losses from the Soil/Plant System: A Review. *Ann. Appl. Biol.* **2013**, *162*, 145−173.

(9) Luo, Y.; Li, H.; Huang, Y.-R.; Zhao, T.-L.; Yao, Q.-Z.; Fu, S.-Q.; Zhou, G.-T. Bacterial Mineralization of Struvite Using MgO as Magnesium Source and Its Potential for Nutrient Recovery. *Chem. Eng. J.* **2018**, *351*, 195−202.

(10) Bouropoulos, N. C.; Koutsoukos, P. G. Spontaneous Precipitation of Struvite from Aqueous Solutions. *J. Cryst. Growth* **2000**, *213*, 381−388.

(11) Ohlinger, K. N.; Young, T. M.; Schroeder, E. D. Predicting Struvite Formation in Digestion. *Water Res.* **1998**, *32*, 3607−3614.

(12) Ronteltap, M.; Maurer, M.; Hausherr, R.; Gujer, W. Struvite precipitation from urine - Influencing factors on particle size. *Water Res.* **2010**, *44*, 2038−2046.

(13) Stratful, I.; Scrimshaw, M. D.; Lester, J. N. Conditions Influencing the Precipitation of Magnesium Ammonium Phosphate. *Water Res.* **2001**, *35*, 4191−4199.

(14) Le Corre, K. S.; Valsami-Jones, E.; Hobbs, P.; Parsons, S. A. Impact of Calcium on Struvite Crystal Size, Shape and Purity. *J. Cryst. Growth* **2005**, *283*, 514−522.

(15) Senbayram, M.; Gransee, A.; Wahle, V.; Thiel, H. Role of magnesium fertilisers in agriculture: plant-soil continuum. *Crop Pasture Sci.* **2015**, *66*, 1219.

(16) Kiani, D.; Sheng, Y.; Lu, B.; Barauskas, D.; Honer, K.; Jiang, Z.; Baltrusaitis, J. Transient Struvite Formation during Stoichiometric (1:1) NH4+ and PO43- Adsorption/Reaction on Magnesium Oxide (MgO) Particles. *ACS Sustainable Chem. Eng.* **2019**, *7*, 1545−1556.

(17) Coluccia, S.; Lavagnino, S.; Marchese, L. Adsorption and Dissociation of Ammonia on the Hydroxylated Surface of Magnesium Oxide Powders. *J. Chem. Soc., Faraday Trans. 1* **1987**, *83*, 477−486.

(18) Tench, A. J.; Giles, D. Infra-red study of the adsorption of ammonia on MgO. Part 2.-The hydrated surface. *J. Chem. Soc., Faraday Trans. 1* **1972**, *68*, 197−201.

(19) Yao, Y.; Gao, B.; Inyang, M.; Zimmerman, A. R.; Cao, X.; Pullammanappallil, P.; Yang, L. Removal of Phosphate from Aqueous Solution by Biochar Derived from Anaerobically Digested Sugar Beet Tailings. *J. Hazard. Mater.* **2011**, *190*, 501−507.

(20) Xia, P.; Wang, X.; Wang, X.; Song, J.; Wang, H.; Zhang, J.; Zhao, J. Struvite crystallization combined adsorption of phosphate and ammonium from aqueous solutions by mesoporous MgO loaded diatomite. *Colloids Surf., A* **2016**, *506*, 220−227.

(21) Li, R.; Wang, J. J.; Zhou, B.; Awasthi, M. K.; Ali, A.; Zhang, Z.; Lahori, A. H.; Mahar, A. Recovery of Phosphate from Aqueous Solution by Magnesium Oxide Decorated Magnetic Biochar and Its Potential as Phosphate-Based Fertilizer Substitute. *Bioresour. Technol.* **2016**, *215*, 209−214.

(22) Zhou, J.; Yang, S.; Yu, J. Facile Fabrication of Mesoporous MgO Microspheres and Their Enhanced Adsorption Performance for Phosphate from Aqueous Solutions. *Colloids Surf., A* **2011**, *379*, 102−108.

(23) Usher, C. R.; Michel, A. E.; Grassian, V. H. Reactions on Mineral Dust. *Chem. Rev.* **2003**, *103*, 4883−4940.

DOI: 10.1021/acs.jpcc.8b12252
J. Phys. Chem. C 2019, 123, 8908−8922

(24) Goodman, A. L.; Bernard, E. T.; Grassian, V. H. Spectroscopic Study of Nitric Acid and Water Adsorption on Oxide Particles: Enhanced Nitric Acid Uptake Kinetics in the Presence of Adsorbed Water. *J. Phys. Chem. A* **2001**, *105*, 6443−6457.

(25) Finocchi, F.; Hacquart, R.; Naud, C.; Jupille, J. Hydroxyl-Defect Complexes on Hydrated MgO Smokes. *J. Phys. Chem. C* **2008**, *112*, 13226−13231.

(26) Costa, D.; Chizallet, C.; Ealet, B.; Goniakowski, J.; Finocchi, F. Water on Extended and Point Defects at MgO Surfaces. *J. Chem. Phys.* **2006**, *125*, 054702.

(27) Alvim, R. S.; Borges, I.; Costa, D. G.; Leitão, A. A. Density-Functional Theory Simulation of the Dissociative Chemisorption of Water Molecules on the MgO(001) Surface. *J. Phys. Chem. C* **2012**, *116*, 738−744.

(28) Taifan, W. E.; Baltrusaitis, J. In Situ Spectroscopic Insights on the Molecular Structure of the MgO/SiO_2 Catalytic Active Sites during Ethanol Conversion to 1,3-Butadiene. *J. Phys. Chem. C* **2018**, *122*, 20894−20906.

(29) Chizallet, C.; Costentin, G.; Che, M.; Delbecq, F.; Sautet, P. Infrared Characterization of Hydroxyl Groups on MgO: A Periodic and Cluster Density Functional Theory Study. *J. Am. Chem. Soc.* **2007**, *129*, 6442−6452.

(30) Di Cosimo, J. I.; Díez, V. K.; Ferretti, C.; Apesteguía, C. R. Basic Catalysis on MgO: Generation, Characterization and Catalytic Properties of Active Sites. *Catalysis*; Royal Society of Chemistry, 2014; Vol. *26*, pp 1−28.

(31) Capdevielle, A.; Sýkorová, E.; Biscans, B.; Béline, F.; Daumer, M.-L. Optimization of Struvite Precipitation in Synthetic Biologically Treated Swine Wastewater-Determination of the Optimal Process Parameters. *J. Hazard. Mater.* **2013**, *244-245*, 357−369.

(32) Stolzenburg, P.; Capdevielle, A.; Teychené, S.; Biscans, B. Struvite Precipitation with MgO as a Precursor: Application to Wastewater Treatment. *Chem. Eng. Sci.* **2015**, *133*, 9−15.

(33) Cruz-Rodrigues, C.; Mecca, T. P.; de Oliveira, D. G.; Ueki, K.; Bueno, O. F. A.; de Macedo, E. C. Physico-Chemical Technologies for Nitrogen Removal from Wastewaters: A Review. *Arq. Bras. Psicolog.* **2015**, *66*, 17−35.

(34) Tench, A. J.; Giles, D. Infra-red study of the adsorption of ammonia on MgO. Part 1.-The dehydrated surface. *J. Chem. Soc., Faraday Trans. 1* **1972**, *68*, 193−196.

(35) Kirinovic, E.; Leichtfuss, A. R.; Navizaga, C.; Zhang, H.; Schuttlefield Christus, J. D.; Baltrusaitis, J. Spectroscopic and Microscopic Identification of the Reaction Products and Intermediates during the Struvite ($MgNH_4PO_4{\cdot}6H_2O$) Formation from Magnesium Oxide (MgO) and Magnesium Carbonate ($MgCO_3$) Microparticles. *ACS Sustainable Chem. Eng.* **2017**, *5*, 1567−1577.

(36) Ishii, S. K. L.; Boyer, T. H. Life Cycle Comparison of Centralized Wastewater Treatment and Urine Source Separation with Struvite Precipitation: Focus on Urine Nutrient Management. *Water Res.* **2015**, *79*, 88−103.

(37) Yetilmezsoy, K.; Sapci-Zengin, Z. Recovery of Ammonium Nitrogen from the Effluent of UASB Treating Poultry Manure Wastewater by MAP Precipitation as a Slow Release Fertilizer. *J. Hazard. Mater.* **2009**, *166*, 260−269.

(38) Rahman, M. M.; Salleh, M. A. M.; Rashid, U.; Ahsan, A.; Hossain, M. M.; Ra, C. S. Production of slow release crystal fertilizer from wastewaters through struvite crystallization - A review. *Arabian J. Chem.* **2014**, *7*, 139−155.

(39) Cai, T.; Park, S. Y.; Li, Y. Nutrient Recovery from Wastewater Streams by Microalgae: Status and Prospects. *Renewable Sustainable Energy Rev.* **2013**, *19*, 360−369.

(40) Zhang, T.; Ding, L.; Ren, H. Pretreatment of Ammonium Removal from Landfill Leachate by Chemical Precipitation. *J. Hazard. Mater.* **2009**, *166*, 911−915.

(41) Lagergreen, S. Zur Theorie Der Sogenannten Adsorption Gelöster Stoffe, Kungliga Svenska Vetenskapsakademiens. *K. Sven. Vetenskapsakad. Handl.* **1907**, *2*, 15−39.

(42) Balouch, A.; Kolachi, M.; Talpur, F. N.; Khan, H.; Bhanger, M. I. Sorption Kinetics, Isotherm and Thermodynamic Modeling of Defluoridation of Ground Water Using Natural Adsorbents. *Am. J. Anal. Chem.* **2013**, *04*, 221−228.

(43) Ho, Y. S.; McKay, G. Pseudo-Second Order Model for Sorption Processes. *Process Biochem.* **1999**, *34*, 451−465.

(44) Gerente, C.; Lee, V. K. C.; Cloirec, P. L.; Mckay, G. Application of Chitosan for the Removal of Metals From Wastewaters by Adsorption-Mechanisms and Models Review. *Crit. Rev. Environ. Sci. Technol.* **2007**, *37*, 41−127.

(45) Fruhwirth, O.; Herzog, G. W.; Hollerer, I.; Rachetti, A. Dissolution and Hydration Kinetics of MgO. *Surf. Technol.* **1985**, *24*, 301−317.

(46) Akao, M.; Marumo, F.; Iwai, S. The Crystal Structure of Hydromagnesite. *Acta Crystallogr., Sect. B: Struct. Crystallogr. Cryst. Chem.* **1974**, *30*, 2670−2672.

(47) Frost, R. L.; Bahfenne, S.; Graham, J. Raman spectroscopic study of the magnesium-carbonate minerals-artinite and dypingite. *J. Raman Spectrosc.* **2009**, *40*, 855−860.

(48) Frost, R. L. Raman Spectroscopic Study of the Magnesium Carbonate Mineral Hydromagnesite ($Mg_5[(CO_3)_4(OH)_2]{\cdot}\,4H_2O$). *J. Raman Spectrosc.* **2011**, *42*, 1690−1694.

(49) Frost, R. L.; Weier, M. L.; Martens, W. N.; Henry, D. A.; Mills, S. J. Raman Spectroscopy of Newberyite, Hannayite and Struvite. *Spectrochim. Acta, Part A* **2005**, *62*, 181−188.

(50) Duffy, T. S.; Meade, C.; Fei, Y.; Mao, H.-K.; Hemley, R. J. High-Pressure Phase Transition in Brucite, $Mg(OH)_2$. *Am. Mineral.* **1995**, *80*, 222−230.

(51) Dawson, P.; Hadfield, C. D.; Wilkinson, G. R. The polarized infra-red and Raman spectra of $Mg(OH)_2$ and $Ca(OH)_2$. *J. Phys. Chem. Solids* **1973**, *34*, 1217−1225.

(52) Prywer, J.; Kasprowicz, D.; Runka, T. Temperature-dependent μ-Raman investigation of struvite crystals. *Spectrochim. Acta, Part A* **2016**, *158*, 18−23.

(53) Qiao, Y.; Feng, J.; Liu, X.; Wang, W. Surface Water PH Variations and Trends in China from 2004 to 2014. *Environ. Monit. Assess.* **2016**, *188*−443. DOI: 10.1007/s10661-016-5454-5

(54) Hao, X.-D.; Wang, C.-C.; Lan, L.; van Loosdrecht, M. C. M. Struvite formation, analytical methods and effects of pH and Ca^{2+}. *Water Sci. Technol.* **2008**, *58*, 1687−1692.

(55) Mejias, J. A.; Berry, A. J.; Refson, K.; Fraser, D. G. The Kinetics and Mechanism of MgO Dissolution. *Chem. Phys. Lett.* **1999**, *314*, 558−563.

(56) Raschman, P.; Fedorockova, A. Dissolution of Periclase in Excess of Hydrochloric Acid: Study of Inhibiting Effect of Acid Concentration on the Dissolution Rate. *Chem. Eng. J.* **2006**, *117*, 205−211.

(57) Vermilyea, D. A. The Dissolution of MgO and $Mg(OH)_2$ in Aqueous Solutions. *J. Electrochem. Soc.* **1969**, *116*, 1179.

(58) Teir, S.; Eloneva, S.; Fogelholm, C.-J.; Zevenhoven, R. Stability of Calcium Carbonate and Magnesium Carbonate in Rainwater and Nitric Acid Solutions. *Energy Convers. Manage.* **2006**, *47*, 3059−3068.

(59) Chou, L.; Garrels, R. M.; Wollast, R. Comparative Study of the Kinetics and Mechanisms of Dissolution of Carbonate Minerals. *Chem. Geol.* **1989**, *78*, 269−282.

(60) Yan, H.; Shih, K. Effects of Calcium and Ferric Ions on Struvite Precipitation: A New Assessment Based on Quantitative X-Ray Diffraction Analysis. *Water Res.* **2016**, *95*, 310−318.

(61) Zhang, T.; Bowers, K. E.; Harrison, J. H.; Chen, S. Impact of Calcium on Struvite Precipitation from Anaerobically Digested Dairy Wastewater. *New Membranes and Advanced Materials for Wastewater Treatment*; American Chemical Society, 2009; Vol. *235*, pp 123−134.

(62) Hutnik, N.; Wierzbowska, B.; Matynia, A. Effect of Inorganic Impurities on Quality of Struvite in Continuous Reaction Crystallization at the Excess of Magnesium Ions. *Przem. Chem.* **2012**, *91*, 762−766.

(63) Acelas, N. Y.; Flórez, E.; López, D. Phosphorus Recovery through Struvite Precipitation from Wastewater: Effect of the Competitive Ions. *Desalin. Water Treat.* **2015**, *54*, 2468−2479.

(64) Zhang, H.; Gong, W.; Luo, X.; Xie, B.; Li, G.; Liang, H. Obtaining High-Purity Struvite from Anaerobically Digested Waste-

water: Effects of PH, Mg/P, and Ca^{2+} Interactions. *Environ. Eng. Sci.* **2019**, *36*, 102−113.

(65) Byrnes, A. P.; Wyllie, P. J. Subsolidus and Melting Relations for the Join $CaCO_3$-$MgCO_3$ at 10 Kbar. *Geochim. Cosmochim. Acta* **1981**, *45*, 321−328.

(66) Achour, A.; Arman, A.; Islam, M.; Zavarian, A. A.; Basim Al-Zubaidi, A.; Szade, J. Synthesis and Characterization of Porous $CaCO_3$ Micro/Nano-Particles. *Eur. Phys. J. Plus* **2017**, *132*, 267−275.

(67) Render, D.; Samuel, T.; King, H.; Vig, M.; Jeelani, S.; Babu, R. J.; Rangari, V. Biomaterial-Derived Calcium Carbonate Nanoparticles for Enteric Drug Delivery. *J. Nanomater.* **2016**, *2016*, 3170248.

(68) De La Pierre, M.; Carteret, C.; Maschio, L.; André, E.; Orlando, R.; Dovesi, R. The Raman Spectrum of $CaCO_3$ polymorphs Calcite and Aragonite: A Combined Experimental and Computational Study. *J. Chem. Phys.* **2014**, *140*, 164509.

(69) Carteret, C.; De La Pierre, M.; Dossot, M.; Pascale, F.; Erba, A.; Dovesi, R. The Vibrational Spectrum of $CaCO_3$ aragonite: A Combined Experimental and Quantum-Mechanical Investigation. *J. Chem. Phys.* **2013**, *138*, 014201.

(70) Yan, J.; Zhao, C. Y. First-principle study of CaO/Ca(OH)2 thermochemical energy storage system by Li or Mg cation doping. *Chem. Eng. Sci.* **2014**, *117*, 293−300.

(71) Padanyi, Z. V. The Raman Spectrum of Ca(OH)2. *Solid State Commun.* **1970**, *8*, 541−543.

(72) Schmid, T.; Dariz, P. Shedding light onto the spectra of lime: Raman and luminescence bands of CaO, $Ca(OH)_2$ and $CaCO_3$. *J. Raman Spectrosc.* **2014**, *46*, 141−146.

(73) Adar, F.; Mamedov, S.; Whitely, A. Limits of Spatial Resolution of a Raman Microscope. *Microsc. Microanal.* **2005**, *11*, 728−729.

(74) Swanson, H. E.; McMurdie, H. F.; Morris, M. C.; Evans, E. H.; Paretzkin, B. Standard X-Ray Diffraction Powder Patterns. *National Bureau of Standards Monograph 25*; Institute for Materials Research National Bureau of Standards: Washington, DC, 1974; pp 1−134.

(75) Kim, J. H.; Kim, S. H.; Kim, H. K.; Akaike, T.; Kim, S. C. Adhesion and growth of endothelial cell on amphiphilic PU/PS IPN surface: Effect of amphiphilic balance and immobilized collagen. *J. Biomed. Mater. Res.* **2002**, *62*, 613−621.

(76) O'Shea, D. C.; Barlett, M. L.; Young, R. A. Compositional Analysis of Apatites with Laser Raman Spectroscopy: (OH , F , Cl) Apatites. *Arch. Oral Biol.* **1974**, *19*, 995−1006.

(77) Fowler, B. O.; Markovic, M.; Brown, W. E. Octacalcium Phosphate. 3. Infrared and Raman Vibrational Spectra. *Chem. Mater.* **1993**, *5*, 1417−1423.

(78) Sauer, G. R.; Zunic, W. B.; Durig, J. R.; Wuthier, R. E. Fourier Transform Raman Spectroscopy of Synthetic and Biological Calcium Phosphates. *Calcif. Tissue Int.* **1994**, *54*, 414−420.

(79) Stammeier, J. A.; Purgstaller, B.; Hippler, D.; Mavromatis, V.; Dietzel, M. In-Situ Raman Spectroscopy of Amorphous Calcium Phosphate to Crystalline Hydroxyapatite Transformation. *Methods* **2018**, *5*, 1241−1250.

(80) Ballirano, P.; De Vito, C.; Mignardi, S.; Ferrini, V. Phase transitions in the $MgCO_2H_2O$ system and the thermal decomposition of dypingite, $Mg_5(CO_3)_4(OH)_2·5H_2O$: Implications for geosequestration of carbon dioxide. *Chem. Geol.* **2013**, *340*, 59−67.

(81) Purgstaller, B.; Konrad, F.; Dietzel, M.; Immenhauser, A.; Mavromatis, V. Control of Mg^{2+}/Ca^{2+} Activity Ratio on the Formation of Crystalline Carbonate Minerals via an Amorphous Precursor. *Cryst. Growth Des.* **2017**, *17*, 1069−1078.

(82) Fleet, M. E.; Liu, X.; King, P. L. Accommodation of the carbonate ion in apatite: An FTIR and X-ray structure study of crystals synthesized at 2-4 GPa. *Am. Mineral.* **2004**, *89*, 1422−1432.